Article:
Chen, W., Fan, Z., Liu, P. et al. (2026) Interfacial chemistry governs nanoparticle self-sorting during biomimetic crystallization. Nature Communications. ISSN: 2041-1723

https://doi.org/10.1038/s41467-026-75685-3

Nature Communications

https://doi.org/10.1038/s41467-026-75685-3

Article in Press

Interfacial chemistry governs nanoparticle self-sorting during biomimetic crystallization

Received: 1 April 2026

Accepted: 6 July 2026

Published online: 04 August 2026

Cite this article as: Chen, W., Fan, Z., Liu, P. *et al.* Interfacial chemistry governs nanoparticle self-sorting during biomimetic crystallization. *Nat Commun* (2026). https://doi.org/10.1038/s41467-026-75685-3

Wenting Chen 雯婷, Zhuodi Fan 范卓迪, Pei Liu 刘配, Xiaohong Hu 胡小 , Yihao Yang 怡豪, Qin Li 李琴, Meijiang Wang 王美江, Jingjing He 何晶晶, Wenjun Zhang 文君, Steven P. Armes & Yin Ning 宁印

Interfacial chemistry governs nanoparticle self-sorting during biomimetic crystallization

Wenting Chen (陈雯婷),[a,b] Zhuodi Fan (范卓迪),[a,b] Pei Liu (刘配),[a,b] Xiaohong Hu (胡小红),*[,a,b,c] Yihao Yang (杨怡豪),[a,b] Qin Li (李琴),[a,b] Meijiang Wang (王美江),[a,b] Jingjing He (何晶晶),[a,b] Wenjun Zhang (张文君)*[, d], Steven P. Armes,*[,e] and Yin Ning (宁印)*[,a,b,c]

[a] State Key Laboratory of Bioactive Molecules and Druggability Assessment, College of Chemistry and Materials Science, Jinan University, Guangzhou 510632, China.

[b] Guangdong Provincial Key Laboratory of Supramolecular Coordination Chemistry, College of Chemistry and Materials Science, Jinan University, Guangzhou 510632, China.

[c] Guangdong Basic Research Center of Excellence for Natural Bioactive Molecules and Discovery of Innovative Drugs, College of Chemistry and Materials Science, Jinan University, Guangzhou 510632, China.

[d] College of Resources and Environment, Huazhong Agricultural University, Wuhan 430070, China.

[e] School of Mathematical and Physical Sciences, University of Sheffield, Brook Hill, Sheffield, South Yorkshire S3 7HF, UK.

E-mail: xiaohonghu@jnu.edu.cn (X.H.); wenjunzhang@mail.hzau.edu.cn (W.Z.); s.p.armes@sheffield.ac.uk (S.P.A.); yinning@jnu.edu.cn (Y.N.)

Abstract

Biominerals comprise composite crystals in which organic constituents are spatially organized within mineral matrices with exquisite precision, giving rise to hierarchically ordered architectures. Despite extensive efforts, achieving precise control over organic–inorganic interactions to construct biomimetic composite materials with programmable composition and spatial organization remains a major challenge. Here we show that diblock copolymer nanoparticles with distinct compositions and dimensions—resembling pseudo-proteins—undergo spontaneous self-sorting during occlusion within growing calcite crystals, yielding artificial biominerals in which two nanoparticle populations are selectively localized in distinct crystalline domains. Using *in situ* monitoring techniques and atomic force microscopy, we demonstrate that this self-sorting process arises from nanoparticle surface chemistry, which leads to differing polymer–mineral interfacial interactions. Moreover, the resulting composite crystals exhibit spatiotemporal release of the occluded species, highlighting the potential for advanced delivery systems. More broadly, self-sorting occlusion establishes a conceptual framework for understanding the spatial organization of organic components in biominerals and provides a versatile strategy for the rational design of next-generation biomimetic materials.

Introduction

In natural biominerals such as bones, teeth or shells, inorganic minerals are not isolated entities but are intricately interwoven with biopolymers (e.g. peptides) to form hierarchical hybrid architectures[1-4]. A striking feature of these systems is that the organic component is spatially partitioned within or around the crystalline domains, rather than merely randomly distributed[5,6]. Such remarkable structures are believed to be indispensable for conferring exceptional stiffness, toughness, and damage tolerance[7]. Thus, mimicking nature to synthesize composite crystals with similar properties has been a hot research topic for a long time[8-12]. Indeed, a few striking examples of synthetic materials designed to rival or even surpass the performance of natural biominerals have been reported[13-15], such as macroscopic artificial pearl-layer-like materials via a mesoscopic-scale approach combining 'assembly and mineralization' [16] and artificial biominerals, exhibiting texture and defect structures similar to those of biogenic calcite crystals, prepared by incorporating anionic block copolymer micelles into a calcite matrix[17].

Notably, prior biomimetic approaches have typically focused on the interaction between single organic components and minerals because using multiple components complicates the identification of causal relationships[18,19]. In contrast, natural biomineralization is usually a much more complex process involving a diverse array of proteins, polysaccharides, lipids, and other organic components[20,21]. To date, multi-component biomimetic studies remain rare, no doubt because it is extremely difficult to distinguish between all the possible interactions over multiple length scales using current analytical techniques. Resolving these challenges would represent a conceptual breakthrough while establishing general principles for organic–inorganic interactions that could transform fields far beyond biomineralization[22,23]. Such advances would not only enhance our fundamental understanding of how living systems achieve nanoscale control over crystalline architectures but also provide essential design principles for the rational synthesis of bioinspired hybrid materials with tailored structure and function[24-26].

In this study, we design nanoparticles with precise surface chemistries and dimensions that serve as tunable surrogates for biomacromolecules and introduce a new experimental model to

elucidate the fundamental parameters governing nanoparticle partitioning and segregation during crystallization. Systematic modulation of chemical functionality, size and morphology, provides important insights into how certain functional groups govern the spatially precise self-sorting occlusion of nanoparticles within an inorganic crystalline matrix. Herein, self-sorting occlusion refers to the spontaneous and selective incorporation of two different guest nanoparticles within distinct regions of the host matrix. Our approach not only offers a useful model for understanding natural biomineralization mechanisms but also establishes a conceptual framework for the spatially controlled integration of organic and inorganic materials, with implications for the design of next-generation biomimetic hybrid materials.

Results

Synthesis and characterization of diblock copolymer nanoparticles. Reversible addition-fragmentation chain transfer (RAFT) polymerization was combined with polymerization-induced self-assembly (PISA) to prepare a series of diblock copolymer nanoparticles with either sulfate-rich or carboxylate-rich surface chemistry. Initially, poly(ammonium 2-sulfatoethyl methacrylate)$_{56}$ and poly(methacrylic acid)$_{54}$ macromolecular chain transfer agents (denoted as S_{56} macro-CTA and M_{54} macro-CTA, respectively; the subscripts denote the mean degree of polymerization in each case) were synthesized by RAFT solution polymerization (Fig. 1a-b, Supplementary Fig. 1 and Supplementary Table 1). Subsequently, these precursors were chain-extended with benzyl methacrylate (B) to form near-monodisperse, sterically-stabilized poly(ammonium 2-sulfatoethyl methacrylate)$_{56}$-*block*-poly(benzyl methacrylate)$_{500}$ [denoted as S_{56}-B_{500}] spheres or poly(methacrylic acid)$_{54}$-*block*-poly(benzyl methacrylate)$_{200}$ [M_{56}-B_{200}] vesicles (Fig. 1c–d and Supplementary Table 2). To facilitate confocal laser scanning microscopy (CLSM) analysis, both types of nanoparticles were fluorescently labeled by incorporating a small amount of either 2-(methacryloyloxy)ethyl thiocarbamoyl rhodamine B (RhBMA) or fluorescein *O*-methacrylate (FMA) into the core-forming poly(benzyl methacrylate) block (Fig. 1a-b). It is worth emphasizing that these nanoparticles were designed to have distinctive morphologies (spheres vs. vesicles, Fig. 1c–d) and sizes (101 ± 27 nm vs. 306 ± 92 nm, Fig. 1e) to aid their

differentiation by electron microscopy. On the other hand, the mean DPs of their steric stabilizer chains (56 vs. 54) were deliberately matched to minimize the known influence of chain length on their occlusion within host crystals[18]. Notably, hydrodynamic diameters determined by dynamic light scattering (DLS, Fig. 1e) were larger than the mean diameters estimated from transmission electron microscopy (TEM, Supplementary Fig. 2). This is because DLS measures the effective size of nanoparticles dispersed in aqueous media, which includes the solvated layer of steric stabilizer chains[27].

Self-sorting occlusion of S_{56}-B_{500} spheres and M_{54}-B_{200} vesicles within calcite. As one of the most abundant minerals, calcite ($CaCO_3$) was selected as a model host crystal[28]. In the absence of any additives, $CaCO_3$ crystallizes to form transparent rhombohedra with smooth surfaces. In contrast, crystals grown in the presence of S_{56}-B_{500} spheres or M_{54}-B_{200} vesicles (or a binary mixture thereof) produced composite crystals with roughened surfaces (Supplementary Fig. 3). To examine their internal structure, argon ion beam etching was employed to expose cross-sections of the composite crystals, followed by field-emission scanning electron microscopy (SEM) analysis. This revealed distinctly different occlusion behavior. S_{56}-B_{500} spheres were incorporated preferentially within the crystal cores, forming well-defined parallelogram-shaped domains aligned with the crystal facets (Fig. 2a–b). In contrast, M_{54}-B_{200} vesicles were predominantly localized near the crystal surface (Fig. 2e–f). Remarkably, self-sorting occurred when both types of nanoparticles were present such that the spheres and vesicles were selectively occluded within the central and surface regions, respectively (Fig. 2i–j). This indicates that the coexistence of S_{56}-B_{500} spheres and M_{54}-B_{200} vesicles does not interfere with their respective preferred occlusion behavior.

CLSM was used to examine the spatial distribution of the S_{56}-B_{500} spheres and M_{54}-B_{200} vesicles within the host crystals. CLSM images confirmed the core localization of S_{56}-B_{500} spheres, the surface localization of M_{54}-B_{200} vesicles, and their self-sorting behavior when employed as binary mixtures (Fig. 2c–d, 2g–h, 2k–l). Notably, fluorescence images recorded for slices of the host crystal provide compelling evidence for self-sorting: the two nanoparticle populations clearly

occupy distinct regions (Fig. 2m and Supplementary Video 1). Importantly, both powder X-ray diffraction (XRD, Supplementary Fig. 4) and Raman spectroscopy (Supplementary Fig. 5) indicated that such nanoparticle occlusion does not alter the host crystal form, which is always calcite.

***In situ* monitoring of the self-sorting occlusion of diblock copolymer nanoparticles.** The composite crystals were precipitated using a well-established ammonia diffusion method (detailed procedure was provided in the **Methods** section)[29]. Upon initiation of crystallization, the solution pH increased rapidly (Fig. 3a), accompanied by a sharp decrease in the calcium ion concentration (Fig. 3b). The pronounced size disparity between the S_{56}-B_{500} spheres and M_{54}-B_{200} vesicles enables their clear differentiation by *in situ* DLS. Hence this technique can be used to track the real-time evolution of both species during the growth of calcite crystals. In addition to size information, the scattered light intensity (or DLS count rate) is directly related to the nanoparticle concentration. As shown in Fig. 3c, the DLS count rate dropped sharply within the first 15 min, which is attributable to the aggregation of M_{54}-B_{200} vesicles. This interpretation is supported by the intensity-weighted hydrodynamic size distribution recorded at t = 15 min, which exhibits two broad peaks (black arrows, Fig. 3d) that are characteristic of aggregation; vesicle aggregation is also corroborated by complementary SEM analysis (red arrow, Fig. 3e). Colloidal stability assays revealed that M_{54}-B_{200} vesicles underwent flocculation when the Ca^{2+} concentration exceeded 3 mM, whereas S_{56}-B_{500} spheres remained stable under the same conditions (Supplementary Fig. 6). Strikingly, the DLS count rate increased gradually between 15 min and 7 h (Fig. 3c), indicating spontaneous redispersion of the vesicle aggregates. This is attributed to the gradual depletion of Ca^{2+} from the aqueous reaction solution during calcite crystallization. At later times, the DLS count rate declined again and eventually reached a limiting value (Fig. 3c), with these observations being consistent with the occlusion of M_{54}-B_{200} vesicles. Indeed, high-resolution SEM analysis of samples extracted at various time points revealed that spheres were continuously occluded from the onset up to approximately 4 h, after which vesicle occlusion commenced (Fig. 3e). Together, these observations provide clear evidence that spheres and vesicles undergo sequential self-sorting

occlusion during calcite crystallization. Furthermore, the in situ DLS data indicate that the characteristic population corresponding to the S_{56}-B_{500} spheres is always detected even during the latter stages of crystallization. This confirms that the S_{56}-B_{500} spherical nanoparticles are still present in solution during occlusion of the M_{54}-B_{200} vesicles within the growing crystals.

Underlying mechanism for self-sorting occlusion. Superficially, the self-sorting occlusion of S_{56}-B_{500} spheres and M_{54}-B_{200} vesicles is attributed to reversible aggregation/redispersion of the latter nanoparticles at high/low Ca^{2+} concentration. However, such behavior raises an interesting question: is the variable colloidal (in)stability of M_{54}-B_{200} vesicles solely responsible, or is there a deeper molecular mechanism at play? Nanoparticle occlusion within inorganic crystals is closely related to their ability to interact intimately with the growing crystal surface[30,31], with a strong surface interaction being essential for overcoming interfacial incompatibility and hence driving occlusion[32]. Both S_{56}-B_{500} spheres and M_{54}-B_{200} vesicles interact with calcite crystals through their respective polyelectrolytic stabilizer chains (S_{56} and M_{54}). To probe these interactions, force spectroscopy experiments were performed using an atomic force microscope (AFM) to compare the interactions of both S_{56}-B_{500} spheres and M_{54}-B_{200} vesicles with the growing calcite ($10\bar{1}4$) crystal face (Fig. 4). First, individual steric stabilizer chains (i.e., S_{56} or M_{54}) were tethered to Au-coated AFM tips (Fig. 4a) and then force-distance curves were recorded as the tip approached and retracted from the growing calcite surface. In each case, retraction curves were fitted using the well-known worm-like chain (WLC) model to extract rupture forces and molecular contour lengths (Fig. 4b–c and Supplementary Fig. 7)[33]. Rupture forces were comparable for both S_{56} and M_{54} (Fig. 4d), but the latter exhibited a longer contour length, indicating stronger binding to the calcite surface (Fig. 4e). Given their similar degrees of polymerization, these AFM studies indicate that anionic M_{54} chains interact more strongly with calcite than S_{56} chains during crystallization.

The underlying mechanism for self-sorting occlusion is clearly complex. Notably, further experiments confirmed that the relatively large S_{30}-B_{300} vesicles (220 ± 73 nm diameter) were occluded within the central region of the calcite crystals (Supplementary Fig. 8), similar to the behavior observed for the relatively small S_{56}-B_{500} spheres (101 ± 27 nm diameter). This

observation indicates that the occlusion behavior of these sulfate-functionalized nanoparticles within calcite crystals is governed neither by the mean DP of their poly(ammonium 2-sulfatoethyl methacrylate) steric stabilizer chains nor by their particle size. Furthermore, the mean DP of the poly(methacrylic acid) chains also does not influence the occlusion behavior. Both M_{36}-B_{200} (220 ± 38 nm) and M_{85}-B_{300} (342 ± 99 nm) vesicles, which comprise shorter and longer steric stabilizer chains respectively, are incorporated as a surface-confined layer within growing calcite crystals (Supplementary Fig. 9), which is consistent with the behavior observed for M_{54}-B_{200} vesicles. Such experiments confirm that the occlusion behavior observed for the two types of nanoparticles is neither influenced by their morphology (i.e., spheres or vesicles) nor by the DP of the steric stabilizer block under the experimental conditions in this study. Furthermore, our previous work has shown that occlusion behavior remains unaffected even when the guest nanoparticles reach micrometer-scale dimensions or exhibit highly anisotropic morphologies (e.g., rod-like structures)[34,35].

The Ca^{2+} concentration is a critical parameter during nanoparticle occlusion. Initially, [Ca^{2+}] = 5 mM but as the calcite crystals are formed the Ca^{2+} ions are progressively depleted from the aqueous reaction solution (Fig. 3b). The Ca^{2+} ions not only serve as a precursor for calcite formation, but also act as ionic bridge between the anionic nanoparticles and the growing calcite crystals, which facilitates nanoparticle occlusion within the host crystal (Fig. 5)[34,36]. Colloidal stability and interfacial interactions are both important, but their roles differ for the two types of nanoparticles and evolve over the course of crystallization. For S_{56}-B_{500} spheres, the sulfate-based anionic stabilizer chains are strong polyelectrolytes with good salt tolerance, thus ensuring that these nanoparticles retain their colloidal stability throughout the entire process. This provides a critical condition for the occlusion of S_{56}-B_{500} spheres (state ①, Fig. 5). However, during the latter stages of calcite growth, the Ca^{2+} concentration decreases substantially (e.g., below 1 mM), weakening the Ca^{2+}-mediated ionic bridging (state ③, Fig. 5). Moreover, the intrinsic interaction between the S_{56} chains and the calcite surface is relatively weak compared with that of the M_{54} chains, as demonstrated by the AFM force measurements (Fig. 4e). Consequently, once the ionic

bridging is diminished, S_{56}-B_{500} spheres exhibit only limited affinity for the growing calcite surface and are no longer efficiently incorporated during subsequent crystal growth. As a result, S_{56}-B_{500} spheres are predominantly retained within the crystal cores, having been occluded during the early stages of crystallization.

The situation is more complex for M_{54}-B_{200} vesicles. At a relatively high Ca^{2+} concentration, M_{54}-B_{200} vesicles form large aggregates and precipitate, therefore occlusion cannot occur (state ②, Fig. 5). However, after a substantial reduction in the Ca^{2+} concentration, these flocculated vesicles undergo spontaneous redispersal to enable the belated occlusion of individual M_{54}-B_{200} vesicles (state ④, Fig. 5). This explains why M_{54}-B_{200} vesicles are predominantly located within the near-surface layer of the calcite crystals. The occlusion of M_{54}-B_{200} vesicles within calcite at such low Ca^{2+} concentrations is attributed to a stronger interaction between the M_{54} steric stabilizer chains and the calcite surface, as demonstrated by the force spectroscopy studies (Fig. 4). Indeed, when the initial Ca^{2+} concentration was reduced to 0.5 mM, M_{54}-B_{200} vesicles could be efficiently occluded, whereas S_{56}-B_{500} spheres were excluded from the calcite crystals (Supplementary Fig. 10). Interestingly, the occlusion behavior of either S_{56}-B_{500} spheres or M_{54}-B_{200} vesicles alone is the same as that observed for a binary mixture of these two species. In other words, the presence of one type of nanoparticle does not influence the occlusion behavior exhibited by the other. Remarkably, an overlap region was identified in which both spheres and vesicles underwent occlusion, particularly when using vesicles bearing a relatively short steric stabilizer block (e.g., M_{36}-B_{200} vesicles, Supplementary Fig. 11).

Universality Study. To examine whether self-sorting occlusion is a generic phenomenon, we performed further experiments. Given that the occlusion behavior of guest nanoparticles is closely governed by their surface chemistry, we posited that, if relatively large guest microparticles were coated with nanoparticles, then the occlusion behavior of the former system should reflect that of the latter. To examine this hypothesis, two new types of diblock copolymer nanoparticles were prepared via RAFT-mediated PISA: poly(potassium 3-sulfopropyl methacrylate)$_{57}$-*block*-poly(styrene-*alt*-*N*-phenylmaleimide)$_{100}$ [SK_{57}-P(St-*alt*-NMI)$_{100}$] spheres and poly(methacrylic

acid)$_{75}$-*block*-poly(styrene-*alt*-*N*-phenylmaleimide)$_{100}$ [M$_{75}$-P(St-*alt*-NMI)$_{100}$] spheres (Supplementary Table 3 and Supplementary Fig. 12). Notably, the sulfonate-based steric stabilizer block was selected for its chemical similarity to the sulfate-based steric stabilizer reported above. Instead of employing SK$_{57}$-P(St-*alt*-NMI)$_{100}$ and M$_{75}$-P(St-*alt*-NMI)$_{100}$ directly for self-sorting occlusion experiments, we electrostatically adsorbed these two types of anionic nanoparticles onto cationic spherical mesoporous silica (MSNs-NH$_2$) and octahedral zirconium-based metal-organic framework (UiO-66-NH$_2$) particles respectively to form core–satellite composite microparticles (Supplementary Fig. 13). If the self-sorting occlusion mechanism is indeed dictated by surface chemistry, these composite particles should exhibit the occlusion behavior of either SK$_{57}$-P(St-*alt*-NMI)$_{100}$ or M$_{75}$-P(St-*alt*-NMI)$_{100}$ based on their respective surface compositions. As anticipated, neither the uncoated MSNs-NH$_2$ nor the uncoated UiO-66-NH$_2$ particles alone underwent occlusion within calcite crystals (Supplementary Fig. 14). However, SK$_{57}$-P(St-alt-NMI)$_{100}$-decorated MSNs-NH$_2$ particles were incorporated within the cores of calcite crystals, whereas M$_{75}$-P(St-*alt*-NMI)$_{100}$-decorated UiO-66-NH$_2$ particles were incorporated into the near-surface layers of calcite crystals (Supplementary Fig. 15a–h). Furthermore, using a binary mixture of these two types of microparticles led to self-sorting occlusion behavior (Supplementary Fig. 15i–l). These nanoparticles with varying sizes and morphologies exhibit consistent occluding behaviors due to their uniform chemical properties on the nanoparticle surfaces. These results further demonstrate that self-sorting occluding is primarily determined by the chemical characteristics of the nanoparticle surfaces, rather than by other factors.

Discussion

There have been many reports on the effect of single-component additives such as soluble (bio)macromolecules or nanoparticles on crystal nucleation and growth[37-40]. The proliferation of such studies is no doubt related to their relative simplicity, which allows straightforward interpretation of causal relationships. In contrast, multi-component additive systems have been rarely studied. Herein, RAFT-mediated PISA provides a robust platform technology for the rational synthesis of S$_{56}$-B$_{500}$ spheres and M$_{54}$-B$_{200}$ vesicles with well-defined surface chemistry and

morphology[41,42]. Such precise control is essential for elucidating the self-sorting occlusion mechanism, as it enables clear differentiation between the two types of nanoparticles when assessing their respective spatial distributions within calcite (Fig. 2). Moreover, it allows the use of *in situ* DLS to monitor the development of self-sorting occlusion during calcite growth (Fig. 3).

This study introduces a new concept that offers valuable physical insights into both natural biomineralization and the design of advanced materials. It is well-established that various organic molecules such as proteins and polysaccharides guide biomineralization by interacting selectively with crystal surfaces[43]. Similarly, nanoparticles bearing differing surface chemistry – sulfate-functionalized S_{56}-B_{500} spheres and carboxylate-functionalized M_{54}-B_{200} vesicles – exhibit distinctive occlusion behavior during calcite crystallization (Fig. 2). This self-sorting behavior closely resembles the selective incorporation of biomolecules in natural biominerals[6,44], whereby specific organic components occupy well-defined crystal domains to achieve hierarchical organization and functional specialization[7,45]. Other forms of self-sorting phenomena have also been reported. For example, in poly(ε-caprolactone) (PCL) spherulites, the degree of crystallinity exhibits a spatial distribution along the radial direction, with lower crystallinity observed at the spherulite center. Consequently, the central region of such spherulites melts at a lower temperature than that of the outer region.[46].

The ability to precisely control the spatial distribution of nanoparticles within an inorganic matrix opens up new avenues for designing artificial biominerals and advanced composite materials[47,48]. A formidable challenge when attempting to replicate natural biomineralization is achieving the selective incorporation of organic components into the mineral matrix. Self-sorting occlusion provides a promising strategy to address this daunting problem, since it potentially enables the formation of synthetic composite crystals with spatially graded distributions of functional groups or biomolecules. By tuning the surface chemistry of nanoparticles, their occlusion can be directed to specific regions of the matrix, leading to hierarchical materials with enhanced toughness, hardness and durability[15,49-51].

Calcium carbonate is both biocompatible and pH-sensitive, making it an attractive carrier

material for controlled delivery[52]. This prompts a key question: can spatiotemporal release be achieved by exploiting the exquisite control over the crystal structure provided by self-sorting occlusion? If acid dissolution of $CaCO_3$ involves a surface etching mechanism, then nanoparticles located at or near the crystal surface should be released first, while those nanoparticles embedded deeper within the lattice should be liberated at a later stage. Such spatiotemporal release would offer a powerful design principle for multifunctional and smart delivery systems. To examine this concept, we monitored the acid-induced release of two types of fluorescently-labeled nanoparticles embedded at distinct spatial locations within calcite crystals using real-time confocal microscopy at pH 4. Sequential release is clearly observed: green vesicles are liberated first, followed by the gradual release of red spherical nanoparticles (Fig. 6 and Supplementary Fig. 16). Hence the self-sorting occlusion reported herein can be harnessed to achieve the programmed release of organic nanoparticles from calcite crystals. Given that such nanoparticles can be loaded with drugs or other actives[53], this proof-of-concept experiment highlights the potential of this strategy for the development of spatiotemporal delivery applications.

In summary, diblock copolymer nanoparticles can undergo spatially-segregated occlusion within calcite single crystals by a self-sorting mechanism. This transforms the traditional random incorporation of nanoparticles into a well-defined programmable process. This behavior is governed by the surface chemistry of the nanoparticles, which dictates their interactions with the growing crystal. Such precise control over nanoscale organization offers important insights for bio-inspired mineralization and suggests new opportunities for the rational design of multifunctional composite crystals, particularly in the context of potential delivery applications. Similar self-sorting mechanisms may also be relevant in the context of natural biomineralization, although verifying this hypothesis would no doubt require substantial further research.

Methods

Synthesis of poly(ammonium 2-sulfatoethyl methacrylate)$_{56}$ macromolecular chain transfer agent (S_{56} macro-CTA)

A round-bottom flask equipped with a magnetic stirrer was charged with a 25% w/v aqueous

solution of SEM monomer (120 g, 0.13 mol, target DP = 50). CPCP (0.74 g, 2.64 mmol) and the ACVA initiator (0.15 g, 528 μmol; [CPCP]/[ACVA] molar ratio = 5.0) were then added after adjusting the solution pH to 6 with 1 M NaOH. The flask was sealed with a rubber septum and the reaction solution was purged with N_2 for 30 min before immersion in a preheated oil bath at 70 °C. Polymerization proceeded for 2 h and was quenched by cooling the flask in an ice/water bath and exposing the reaction mixture to air. The resulting polymer was dissolved in methanol and filtered to remove residual insoluble monomer; the filtrate was subsequently added dropwise into excess dichloromethane under continuous stirring to precipitate the polymer. The solvent was carefully decanted, and the precipitate was redissolved in water and freeze-dried overnight to yield the macro-CTA. A mean degree of polymerization (DP) of 56 was determined by ^{1}H NMR spectroscopy, based on the integrated signal intensity of the methacrylic backbone relative to that of the aromatic protons. The synthesis of S_{30} macro-CTA was slightly modified by changing the target DP as 30. The synthetic procedure and GPC data are summarized in Supplementary Table 1.

Synthesis of poly(methacrylic acid)$_{54}$ macromolecular chain transfer agent (M_{54} macro-CTA)

A round-bottomed flask was charged with MAA (20.0 g, 232.4 mmol; target DP = 70), CPCP (0.93 g, 3.3 mmol), ACVA initiator (186 mg, 0.66 mmol; [CPCP]/[ACVA] molar ratio = 5.0), and ethanol (31.4 g). The flask was sealed, degassed under nitrogen for 30 min at 0 °C, and then immersed in a preheated oil bath at 70 °C for 3 h. The polymerization was quenched by cooling the reaction mixture in an ice bath and exposing it to air. The crude polymer was purified by three successive precipitations into a ten-fold excess of diethyl ether. The purified macro-CTA was finally dissolved in water and lyophilized to afford a pink powder. The mean DP of the macro-CTA was determined by ^{1}H NMR spectroscopy, based on the integrated signal intensity of the methacrylic backbone relative to that of the aromatic protons. The synthetic procedure and GPC data are summarized in Supplementary Table 1.

Synthesis of poly(ammonium 2-sulfatoethyl methacrylate)$_{56}$-block-poly(benzyl methacrylate)$_{500}$ (S_{56}-B_{500}) block copolymer spheres labeled with rhodamine via RAFT dispersion polymerization

S_{56} macro-CTA (195 mg, 15 μmol), ACVA (0.84 mg, 3 μmol, [S_{56} macro-CTA]/[ACVA] molar ratio = 5.0), 1:2 w/w water/ethanol (13.6 g), RhBMA (4.9 mg, 7.5 μmol) and BzMA monomer (1.322 g, 7.5 mmol, target DP = 500) were added to a reaction flask. The flask was then sealed, purged with nitrogen for 30 min, and immersed in a preheated oil bath at 70 °C for 24 h. The copolymerization was terminated by cooling the reaction flask using an ice bath and exposing the reaction mixture to air. The resulting S_{56}-B_{500} block copolymer spheres were purified by dialysis against deionized water for 3 days using dialysis tubing with a molecular weight cut-off of 25,000 Da.

Synthesis of poly(methacrylic acid)$_x$-block-poly(benzyl methacrylate)$_y$ (M_x-B_y) block copolymer vesicles labeled with fluorescein via RAFT dispersion polymerization

A representative protocol for the synthesis of M_{54}-B_{200} vesicles was as follows. M_{54} macro-CTA (99.7 mg, 20 μmol), ACVA initiator (1.1 mg, 4 μmol; [M_{54} macro-CTA]/[ACVA] molar ratio = 5.0), fluorescein methacrylate (FMA, 4.0 mg, 10 μmol), and 70:30 w/w methanol/ethanol (4.6 g) were added to a 10 mL glass vial equipped with a magnetic stir bar. Benzyl methacrylate (BzMA, 704.8 mg, 4.0 mmol; target DP = 200) was subsequently added to afford a 15% w/w solution. The vial was sealed and degassed under nitrogen for 30 min at 0 °C, then immersed in an oil bath at 70 °C for 24 h. ^{1}H NMR analysis confirmed a final BzMA conversion of more than 99%. The resulting M_{54}-B_{200} vesicles were diluted to 0.2% w/w and transferred into water by five centrifugation–redispersion cycles (15 min at 9500 rpm per cycle). Synthetic protocols for the other diblock copolymer nanoparticles are summarized in Supplementary Table 2.

Precipitation of calcium carbonate crystals in the presence of various block copolymer additives

Calcium carbonate crystals were precipitated using the ammonia diffusion method[29]. A Petri dish containing 10 mL of a 5 mM $CaCl_2$ aqueous solution plus 0.05% w/w copolymer nanoparticles was placed in a desiccator. Glass slides (pre-cleaned using piranha solution) were positioned at the base of the Petri dish. Crystallization was induced by exposure to ammonium carbonate (2 g, placed at the bottom of the desiccator) for 24 h at 20 °C. Ammonium carbonate decomposes slowly to generate CO_2 and NH_3, which diffuse across the gas–liquid interface into the solution. Dissolved

CO_2 reacts with water to form carbonic acid, which subsequently forms carbonate and bicarbonate ions, whose relative concentrations are governed by the solution pH. Concurrently, dissolved NH_3 increases the solution pH. In the presence of Ca^{2+} ions, these processes produce a solution that is supersaturated with respect to $CaCO_3$. After crystallization, the glass slides were removed, washed three times with deionized water, and rinsed three times with ethanol. Each occlusion experiment was repeated at least twice, with consistent results being obtained.

Data availability

The data that support the findings of this study are available in the paper and its Supplementary Information or from the corresponding author upon request. Source data are provided with this paper.

References

1. Kalmar, L., Homola, D., Varga, G. & Tompa, P. Structural disorder in proteins brings order to crystal growth in biomineralization. *Bone* **51**, 528-534 (2012).
2. Beniash, E. Biominerals—hierarchical nanocomposites: the example of bone. *WIRES Nanomed. Nanobi.* **3**, 47-69 (2011).
3. Sharma, V., Srinivasan, A., Nikolajeff, F. & Kumar, S. Biomineralization process in hard tissues: The interaction complexity within protein and inorganic counterparts. *Acta Biomater.* **120**, 20-37 (2021).
4. Mann, S. *Biomineralization: principles and concepts in bioinorganic materials chemistry*. 210 (Oxford University Press, U.S.A., 2001).
5. Weiner, S. & Addadi, L. Design strategies in mineralized biological materials. *J. Mater. Chem.* **7**, 689-702 (1997).
6. Kitajima, T. & Urakami, H. Differential distribution of spicule matrix proteins in the sea urchin embryo skeleton. *Develop. Growth Differ.* **42**, 295-306 (2000).
7. Mann, S. Molecular recognition in biomineralization. *Nature* **332**, 119-124 (1988).
8. Weber, E. *et al.* Incorporation of a Recombinant Biomineralization Fusion Protein into the Crystalline Lattice of Calcite. *Chem. Mater.* **26**, 4925-4932 (2014).
9. Lang, A. *et al.* Bioinspired Molecular Bridging in a Hybrid Perovskite Leads to Enhanced Stability and Tunable Properties. *Adv. Funct. Mater.* **30**, 2005136 (2020).
10. Liu, Y. *et al.* Functionalizing Single Crystals: Incorporation of Nanoparticles Inside Gel-Grown Calcite Crystals. *Angew. Chem.* **126**, 4211-4215 (2014).

11. Ren, J., Liu, Y. & Li, H. Incorporating polymers within a single-crystal: From heterogeneous structure to multiple functions. *J. Polym. Sci.* **60**, 1151-1173 (2022).
12. Gao, F., Ren, J., Jin, X., Deng, X. & Li, H. Isotropically Dyed Single Crystals Produced via Gel-Incorporation. *ACS Materials Lett.* **4**, 1207-1213 (2022).
13. Yang, T. *et al.* A damage-tolerant, dual-scale, single-crystalline microlattice in the knobby starfish, Protoreaster nodosus. *Science* **375**, 647-652 (2022).
14. Morgan, S., Poundarik, A. A. & Vashishth, D. Do non-collagenous proteins affect skeletal mechanical properties? *Calcif. Tissue Int.* **97**, 281-291 (2015).
15. Kim, Y.-Y. *et al.* Tuning hardness in calcite by incorporation of amino acids. *Nat. Mater.* **15**, 903-910 (2016).
16. Mao, L.-B. *et al.* Synthetic nacre by predesigned matrix-directed mineralization. *Science* **354**, 107-110 (2016).
17. Kim, Y.-Y. *et al.* An artificial biomineral formed by incorporation of copolymer micelles in calcite crystals. *Nat. Mater.* **10**, 890-896 (2011).
18. Ning, Y., Han, L., Derry, M. J., Meldrum, F. C. & Armes, S. P. Model Anionic Block Copolymer Vesicles Provide Important Design Rules for Efficient Nanoparticle Occlusion within Calcite. *J. Am. Chem. Soc.* **141**, 2557-2567 (2019).
19. Ning, Y. *et al.* What dictates the spatial distribution of nanoparticles within calcite? *J. Am. Chem. Soc.* **141**, 2481-2489 (2019).
20. Mann, S. Biomineralization and biomimetic materials chemistry. *J. Mater. Chem.* **5**, 935-946 (1995).
21. Gilbert, P. U. P. A. *et al.* Biomineralization: Integrating mechanism and evolutionary history. *Sci. Adv.* **8**, eabl9653 (2022).
22. Estroff, L. A. Introduction: biomineralization. *Chem. Rev.* **108**, 4329-4331 (2008).
23. Lowenstam, H. A. & Weiner, S. *On Biomineralization*. (Oxford University Press, 1989).
24. Ning, Y. & Armes, S. P. Efficient Occlusion of Nanoparticles within Inorganic Single Crystals. *Acc. Chem. Res.* **53**, 1176-1186 (2020).
25. Nudelman, F. & Sommerdijk, N. A. Biomineralization as an inspiration for materials chemistry. *Angew. Chem, Int. Ed.* **51**, 6582-6596 (2012).
26. Li, H., Xin, H. L., Muller, D. A. & Estroff, L. A. Visualizing the 3D Internal Structure of Calcite Single Crystals Grown in Agarose Hydrogels. *Science* **326**, 1244-1247 (2009).
27. Yang, D. *et al.* Liquid–Solid Interfacial Fusion Assembly Enables the Precision Fabrication of Block Copolymer Vesicles. *Adv. Mater.* **38**, e14207 (2026).
28. Meldrum, F. C. & Cölfen, H. The many lives of calcium carbonate. *Nat. Chem.* **15**, 1196-1196 (2023).

29. Ihli, J., Bots, P., Kulak, A., Benning, L. G. & Meldrum, F. C. Elucidating Mechanisms of Diffusion-Based Calcium Carbonate Synthesis Leads to Controlled Mesocrystal Formation. *Adv. Funct. Mater.* **23**, 1965-1973 (2013).
30. Hendley IV, C. T. *et al.* Mechanistic insights into diblock copolymer nanoparticle–crystal interactions revealed via in situ atomic force microscopy. *J. Am. Chem. Soc.* **140**, 7936-7945 (2018).
31. Rae Cho, K. *et al.* Direct observation of mineral–organic composite formation reveals occlusion mechanism. *Nat. Commun.* **7**, 10187 (2016).
32. Muñoz-Espí, R., Qi, Y., Lieberwirth, I., Gomez, C. M. & Wegner, G. Surface-Functionalized Latex Particles as Controlling Agents for the Mineralization of Zinc Oxide in Aqueous Medium. *Chem. -Eur. J.* **12**, 118-129 (2006).
33. Friddle, R. W., Noy, A. & De Yoreo, J. J. Interpreting the widespread nonlinear force spectra of intermolecular bonds. *Proc. Natl. Acad. Sci. U. S. A.* **109**, 13573-13578 (2012).
34. Chen, W. *et al.* Spatioselective Occlusion of Copolymer Nanoparticles within Calcite Crystals Generates Organic-Inorganic Hybrid Materials with Controlled Internal Structures. *Angew. Chem. Int. Ed.* **63**, e202410908 (2024).
35. Ning, Y., Meldrum, F. C. & Armes, S. P. Efficient occlusion of oil droplets within calcite crystals. *Chem. Sci.* **10**, 8964-8972 (2019).
36. Ning, Y. *et al.* Occlusion of sulfate-based diblock copolymer nanoparticles within calcite: effect of varying the surface density of anionic stabilizer chains. *J. Am. Chem. Soc.* **138**, 11734-11742 (2016).
37. Kulak, A. N. *et al.* Continuous structural evolution of calcium carbonate particles: a unifying model of copolymer-mediated crystallization. *J. Am. Chem. Soc.* **129**, 3729-3736 (2007).
38. Chen, J. *et al.* Nanocluster-Induced Liquid-like Precursor Formation and Crystallization: In Situ Visualization and 3D Reconstruction. *J. Am. Chem. Soc.* **147**, 9590-9600 (2025).
39. Metzler, R. A., Tribello, G. A., Parrinello, M. & Gilbert, P. U. P. A. Asprich Peptides Are Occluded in Calcite and Permanently Disorder Biomineral Crystals. *J. Am. Chem. Soc.* **132**, 11585-11591 (2010).
40. De Yoreo, J. J. *et al.* Crystallization by particle attachment in synthetic, biogenic, and geologic environments. *Science* **349**, aaa6760 (2015).
41. Warren, N. J. & Armes, S. P. Polymerization-Induced Self-Assembly of Block Copolymer Nano-objects via RAFT Aqueous Dispersion Polymerization. *J. Am. Chem. Soc.* **136**, 10174-10185 (2014).
42. D'Agosto, F., Rieger, J. & Lansalot, M. RAFT-Mediated Polymerization-Induced Self-Assembly. *Angew. Chem. Int. Ed.* **59**, 8368-8392 (2020).

43. Arias, J. L. & Fernández, M. S. Polysaccharides and Proteoglycans in Calcium Carbonate-based Biomineralization. *Chem. Rev.* **108**, 4475-4482 (2008).
44. Kahr, B. & Gurney, R. W. Dyeing crystals. *Chem. Rev.* **101**, 893-952 (2001).
45. Addadi, L. & Weiner, S. Interactions between acidic proteins and crystals: stereochemical requirements in biomineralization. *PNAS* **82**, 4110-4114 (1985).
46. Yang, Y., Chen, M., Li, H. & Li, H. The degree of crystallinity exhibiting a spatial distribution in polymer films. *Eur. Polym. J.* **107**, 303-307 (2018).
47. Ning, Y. *et al.* Spatially controlled occlusion of polymer-stabilized gold nanoparticles within ZnO. *Angew. Chem. Int. Ed.* **58**, 4302–4307 (2019).
48. Yu, B. *et al.* Spatially Engineering the Internal Microstructure of a Single Crystal via Nanoparticle Occlusion. *Angew. Chem. Int. Ed.* **64**, e202505637 (2025).
49. Kim, Y.-Y. *et al.* Hydroxyl-rich macromolecules enable the bio-inspired synthesis of single crystal nanocomposites. *Nat. Commun.* **10**, 5682 (2019).
50. Zhao, Z. *et al.* Interfacial Supra-Assembly of Copolymer Nanoparticles Enables the Formation of Nanocomposite Crystals with a Tunable Internal Structure. *J. Am. Chem. Soc.* **145**, 21546-21553 (2023).
51. Zhang, J. *et al.* Hidden Functional Nanoparticles in Semiconductor Crystals. *J. Am. Chem. Soc.* **148**, 20888-20897 (2026).
52. Han, J. *et al.* Long-acting IL-2 release from pressure-fused biomineral tablets promotes antitumor immune response. *Nat. Cancer* **6**, 1384-1399 (2025).
53. Deng, R., Derry, M. J., Mable, C. J., Ning, Y. & Armes, S. P. Using Dynamic Covalent Chemistry To Drive Morphological Transitions: Controlled Release of Encapsulated Nanoparticles from Block Copolymer Vesicles. *J. Am. Chem. Soc.* **139**, 7616-7623 (2017).

Acknowledgements

We thank Mr. Q. Sun for his assistance in SEM sample preparation and HRSEM imaging. We also acknowledge Cordouan Technologies SAS for providing the instrument used in the *in situ* DLS measurements.

Funding statement

This work was financially supported by the National Natural Science Foundation of China (22475084, 42577022), Guangdong Basic and Applied Basic Research Foundation

(2024A1515012114 and 2025A1515012931), and Science and Technology Project in Guangzhou (202102070001). Y.N. and S.P.A. also thank EPSRC for financial support (EP/P005241/1).

Author contributions

Y.N. conceived the research and acquired funding. Y.N., X.H., and S.P.A. supervised the project. W.C. designed and performed most experiments and analyzed the data. P.L. synthesized the composite nanoparticles and conducted the occlusion experiments. Y.Y. and Q.L. performed TEM imaging, Z.F. assisted with GPC testing. M.W. and J.H. conducted NMR and Raman spectroscopy. W.Z. conducted AFM measurements and analyzed the data. W.C., S.P.A., and Y.N. co-wrote the manuscript. All authors discussed the results and approved the final version.

Competing interests

The authors declare no competing interests.

Figure legends

Fig. 1 | Controlled synthesis of diblock copolymer spheres or vesicles via RAFT-mediated PISA. a, Synthetic protocol for the preparation of rhodamine-functionalized poly(ammonium 2-sulfatoethyl methacrylate)$_{56}$-*block*-poly(benzyl methacrylate)$_{500}$ [S_{56}-B_{500}] spheres; **b,** Synthetic protocol for the preparation of fluorescein-functionalized poly(methacrylic acid)$_{54}$-*block*-poly(benzyl methacrylate)$_{200}$ [M_{54}-B_{200}] vesicles; **c,** TEM image of S_{56}-B_{500} spheres; **d,** TEM image of M_{54}-B_{200} vesicles. The dashed circles indicate individual vesicles. Their apparent aggregation is attributed to drying artifacts arising during TEM sample preparation; **e,** Particle size distributions for S_{56}-B_{500} spheres and M_{54}-B_{200} vesicles obtained from dynamic light scattering (DLS). Cartoons in **c** and **d** (top right) illustrate the corresponding copolymer morphologies.

Fig. 2 | Self-sorting of S_{56}-B_{500} spheres and M_{54}-B_{200} vesicles within a calcite host crystal. These composite crystals were prepared in the presence of various additives: **a-d**, S_{56}-B_{500} spheres; **e-h,** M_{54}-B_{200} vesicles; **i-l,** a binary mixture of S_{56}-B_{500} spheres and M_{54}-B_{200} vesicles. **a-b, e-f, i-j,** Representative high-resolution SEM images of crystal cross-sections prepared by argon ion beam etching. For clarity, spheres and vesicles are pseudo-colored in red and green, respectively. **c, g, k**, CLSM images of the composite crystals showing the spatial distribution of S_{56}-B_{500} spheres (red) and M_{54}-B_{200} vesicles (green). **d, h, l,** Corresponding fluorescence intensity line-scan profiles. **m,** Representative confocal fluorescence slices recorded at regular depths along the z-axis, revealing the localization of two distinct dye-labeled nanoparticles within a single composite crystal. Red fluorescence corresponds to RhBMA-labeled S_{56}-B_{500} spheres, while green fluorescence denotes fluorescein-labeled M_{54}-B_{200} vesicles.

Fig. 3 | *In situ* monitoring of the self-sorting occlusion of S_{56}-B_{500} spheres and M_{54}-B_{200} vesicles during calcite crystal growth. a, pH evolution during calcite crystallization; the inset highlights the initial 0–15 min period. **b,** Variation of Ca^{2+} concentration as a function of crystallization time; the inset shows the 2–14 h interval. **c,** DLS count rate as a function of time, with an inset showing the initial 0–15 min period. Variations in count rate reflect changes in nanoparticle concentration in solution during crystal growth. **d,** Z-average hydrodynamic diameters recorded at selected time points, where substantial shifts in the size distribution indicate subtle changes in colloidal stability. **e,** SEM images of composite crystals recorded at the different time points, highlighting their surface morphology and internal structure. These data indicate the initial occlusion of S_{56}-B_{500} spheres followed by the occlusion of M_{54}-B_{200} vesicles over longer time scales, leading to their spatially segregated occlusion within calcite crystals via a self-sorting mechanism.

Fig. 4 | AFM-based force spectroscopy studies of polymer–calcite interactions in supersaturated

solution (σ = 0.274). a, Schematic representation of a force spectroscopy experiment, in which a single polymer chain (either M_{54} or S_{56}) is tethered to an Au-modified AFM tip. Measurement of force–distance curves acquired with an AFM is used to probe the precise interaction between a single anionic steric stabilizer chain and the calcite surface. **b–c**, Representative force–distance curves showing the interaction of (**b**) S_{56} and (**c**) M_{54} with the surface of a growing calcite crystal. **d–e**, Statistical analysis of (**d**) rupture forces and (**e**) contour lengths for such polymer–calcite interactions. Error bars in (**d–e**) represent standard deviations calculated from ten independent measurements (n = 10).

Fig. 5 | Schematic representation of the self-sorting occlusion mechanism for S_{56}-B_{500} spheres and M_{54}-B_{200} vesicles within calcite crystals. The progressive reduction in the solution concentration of Ca^{2+} during the formation of calcite crystals influences the occlusion behavior for these two types of nanoparticles. The high initial [Ca^{2+}] ensures that only the colloidally stable S_{56}-B_{500} spheres are occluded (mediated by sufficiently strong S_{56}–calcite interactions under high [Ca^{2+}]), whereas the M_{54}-B_{200} vesicles undergo flocculation and are excluded. However, spontaneous redispersion of these aggregated M_{54}-B_{200} vesicles occurs as the [Ca^{2+}] is reduced, which enables their efficient occlusion (II). Notably, the occlusion of S_{56}-B_{500} spheres terminates at lower [Ca^{2+}], whereas that of M_{54}-B_{200} vesicles persists, owing to the stronger interaction of M_{54} steric stabilizer chains with the calcite surface compared to S_{56} chains, as evidenced by AFM force–distance measurements. This difference gives rise to the self-sorting occlusion behavior (III).

Fig. 6 | pH-triggered sequential release of vesicles and spheres monitored by CLSM in pH 4 buffer. **a,** Bright-field images acquired at selected time points. **b,** Corresponding CLSM images. The green fluorescence from M_{54}-B_{200} vesicles progressively diminishes (0→50 min), followed by the gradual loss of red fluorescence from S_{56}-B_{500} spheres (50→100 min), demonstrating the programmable, sequential release of two distinct species occluded at differing locations within the composite crystal.

a

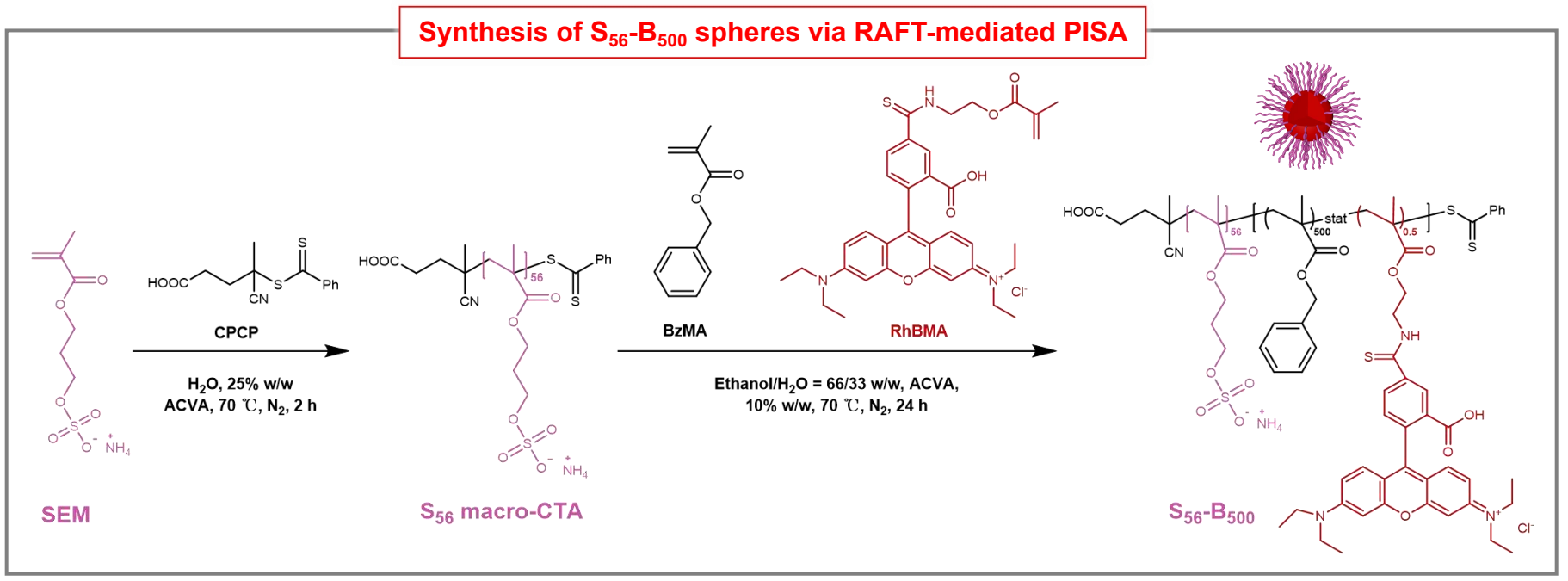
Synthesis of S56-B500 spheres via RAFT-mediated PISA
CPCP
H2O, 25% w/w
ACVA, 70 ℃, N2, 2 h
BzMA
RhBMA
Ethanol/H2O = 66/33 w/w, ACVA,
10% w/w, 70 ℃, N2, 24 h
SEM
S56 macro-CTA
S56-B500

b

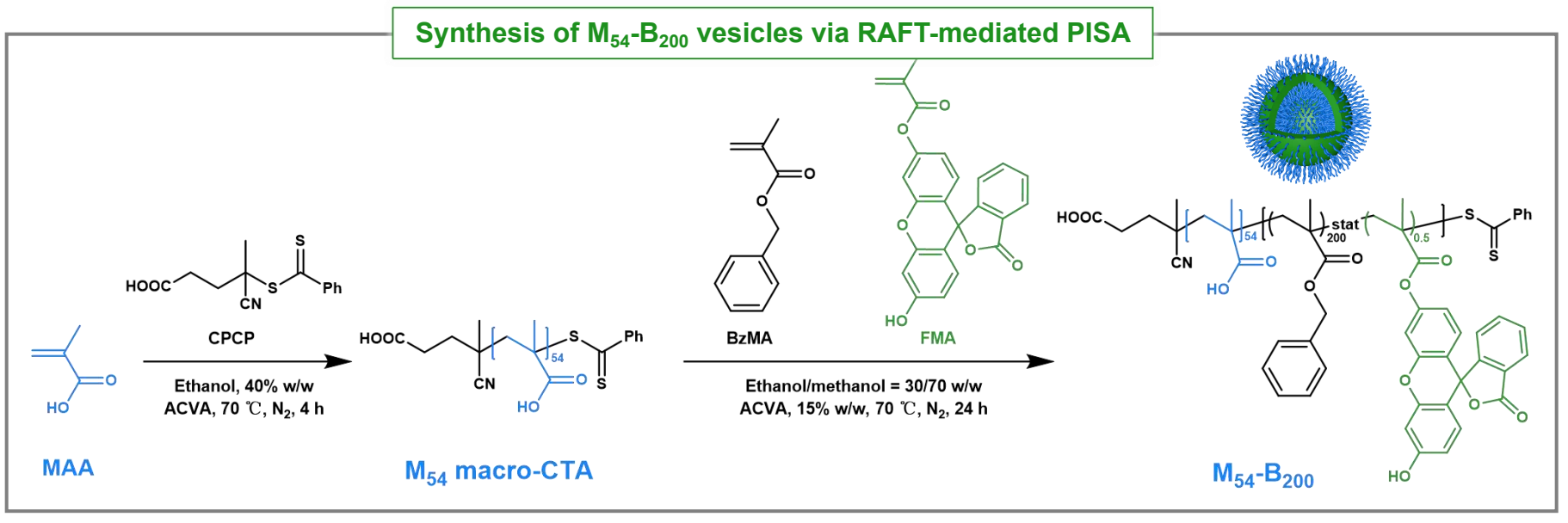
Synthesis of M54-B200 vesicles via RAFT-mediated PISA
CPCP
Ethanol, 40% w/w
ACVA, 70 ℃, N2, 4 h
BzMA
FMA
Ethanol/methanol = 30/70 w/w
ACVA, 15% w/w, 70 ℃, N2, 24 h
MAA
M54 macro-CTA
M54-B200

c

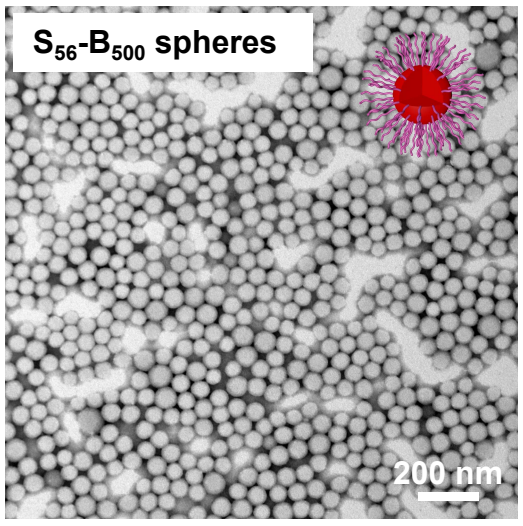
S56-B500 spheres
200 nm

d

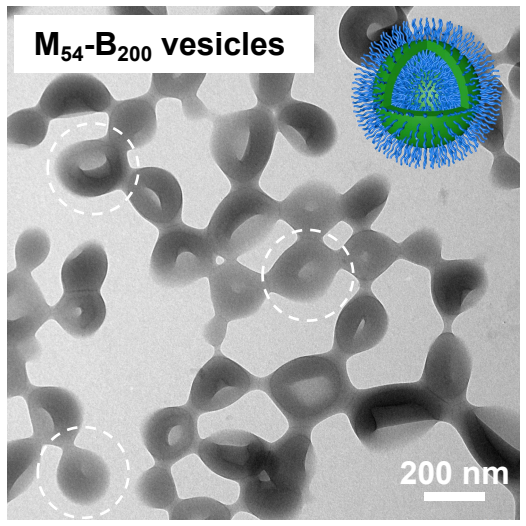
M54-B200 vesicles
200 nm

e

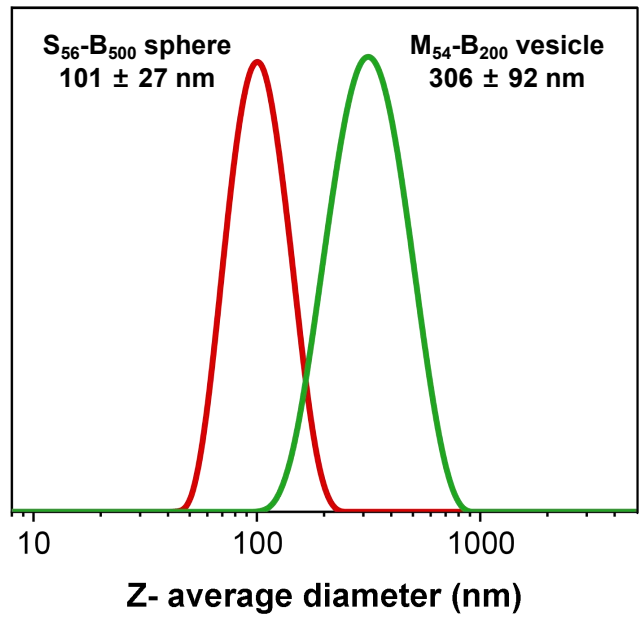
S56-B500 sphere
101 ± 27 nm
M54-B200 vesicle
306 ± 92 nm
10
100
1000
Z- average diameter (nm)

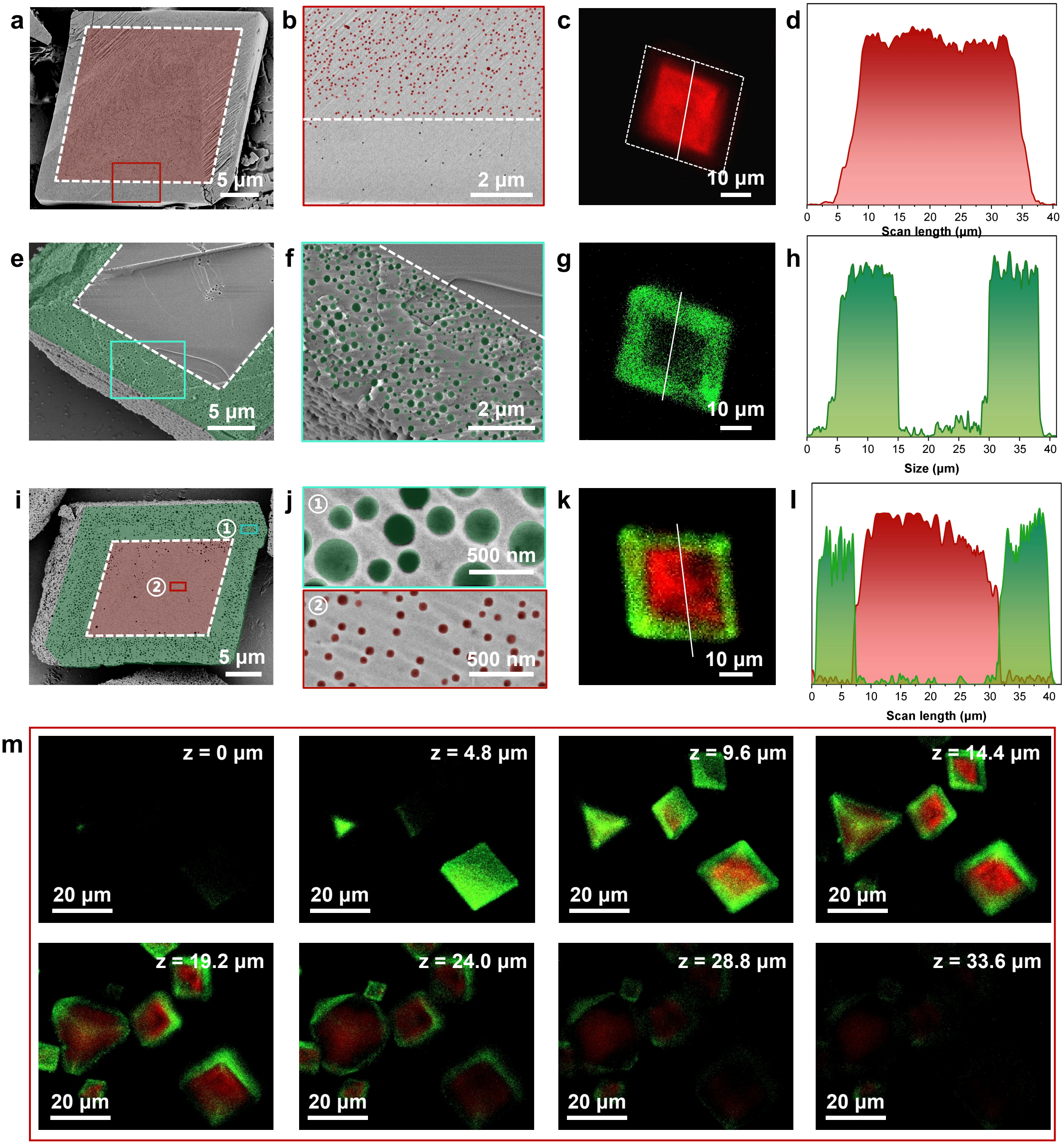
a
5 μm
b
2 μm
c
10 μm
d
0 5 10 15 20 25 30 35 40
Scan length (μm)
e
5 μm
f
2 μm
g
10 μm
h
0 5 10 15 20 25 30 35 40
Size (μm)
i
1
2
5 μm
j
1
500 nm
2
500 nm
k
10 μm
l
0 5 10 15 20 25 30 35 40
Scan length (μm)
m
z = 0 μm
z = 4.8 μm
z = 9.6 μm
z = 14.4 μm
z = 19.2 μm
z = 24.0 μm
z = 28.8 μm
z = 33.6 μm
20 μm

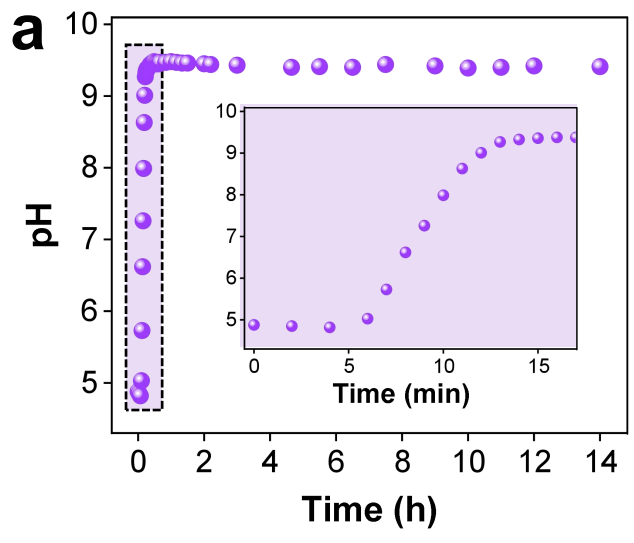
a
pH
Time (h)
Time (min)

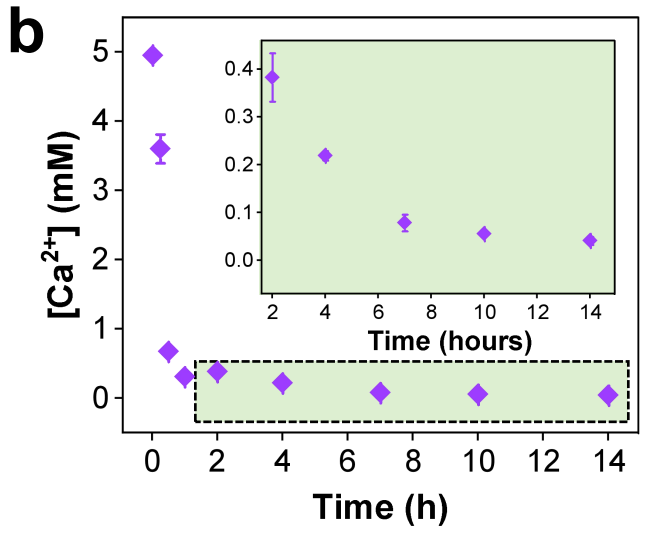
b
[Ca2+] (mM)
Time (h)
Time (hours)

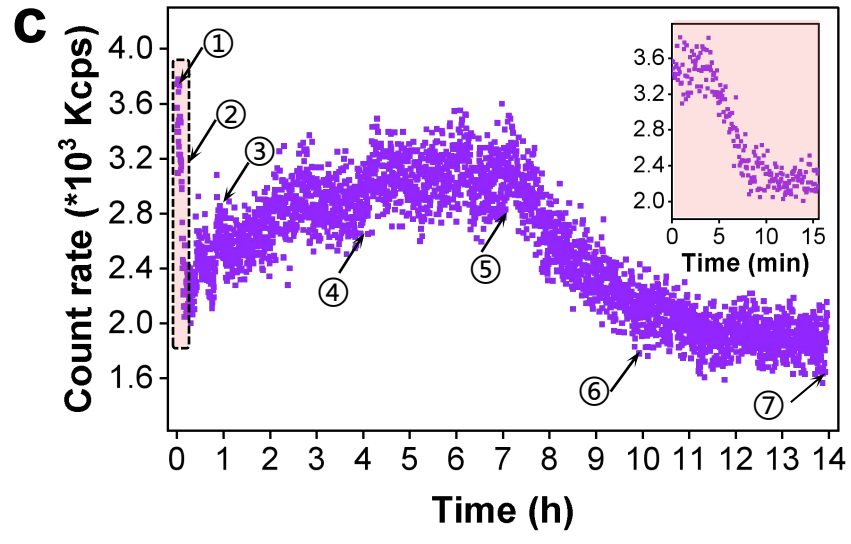
c
Count rate (*10³ Kcps)
Time (h)
Time (min)
①
②
③
④
⑤
⑥
⑦

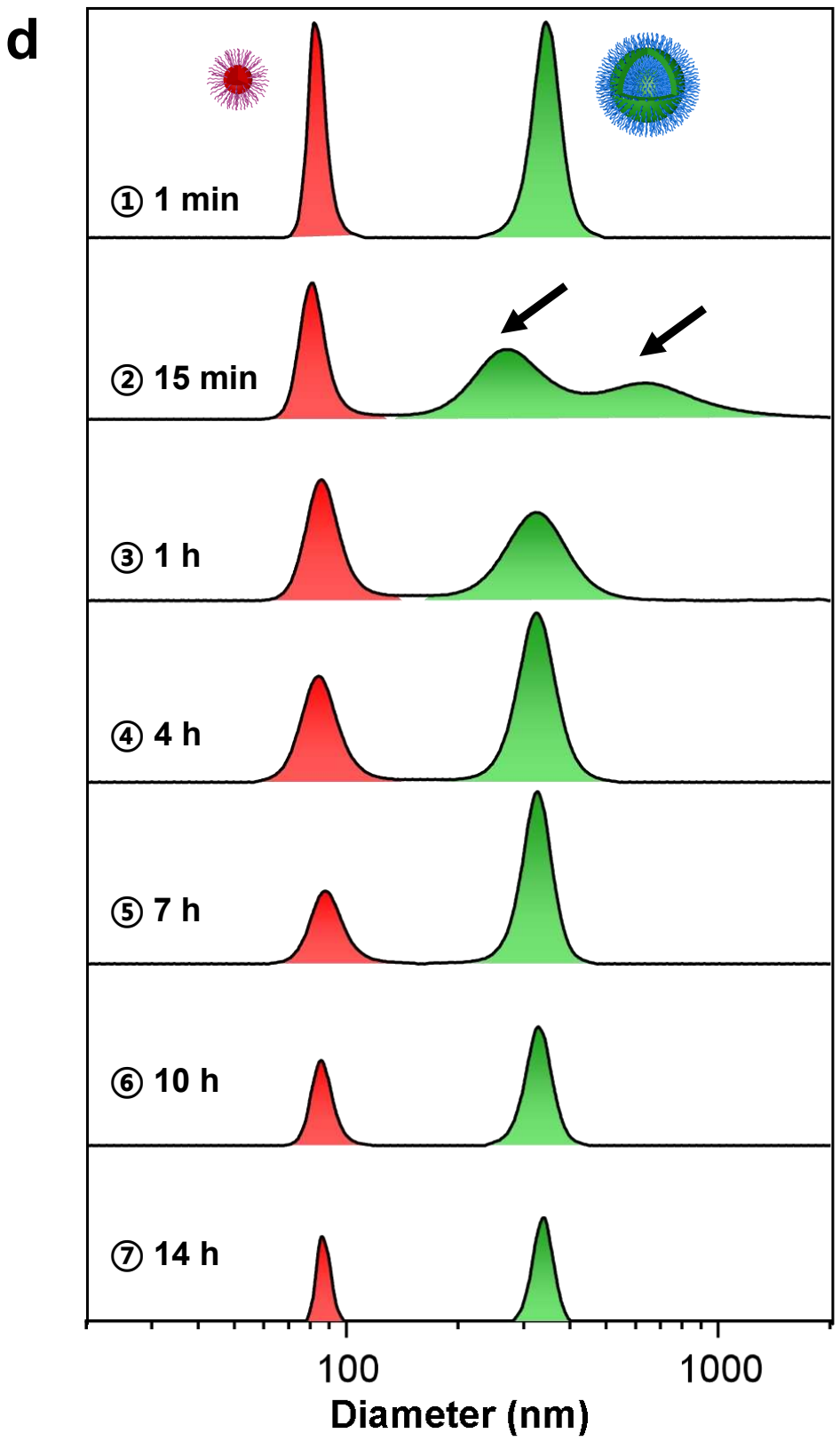
d
① 1 min
② 15 min
③ 1 h
④ 4 h
⑤ 7 h
⑥ 10 h
⑦ 14 h
100
1000
Diameter (nm)

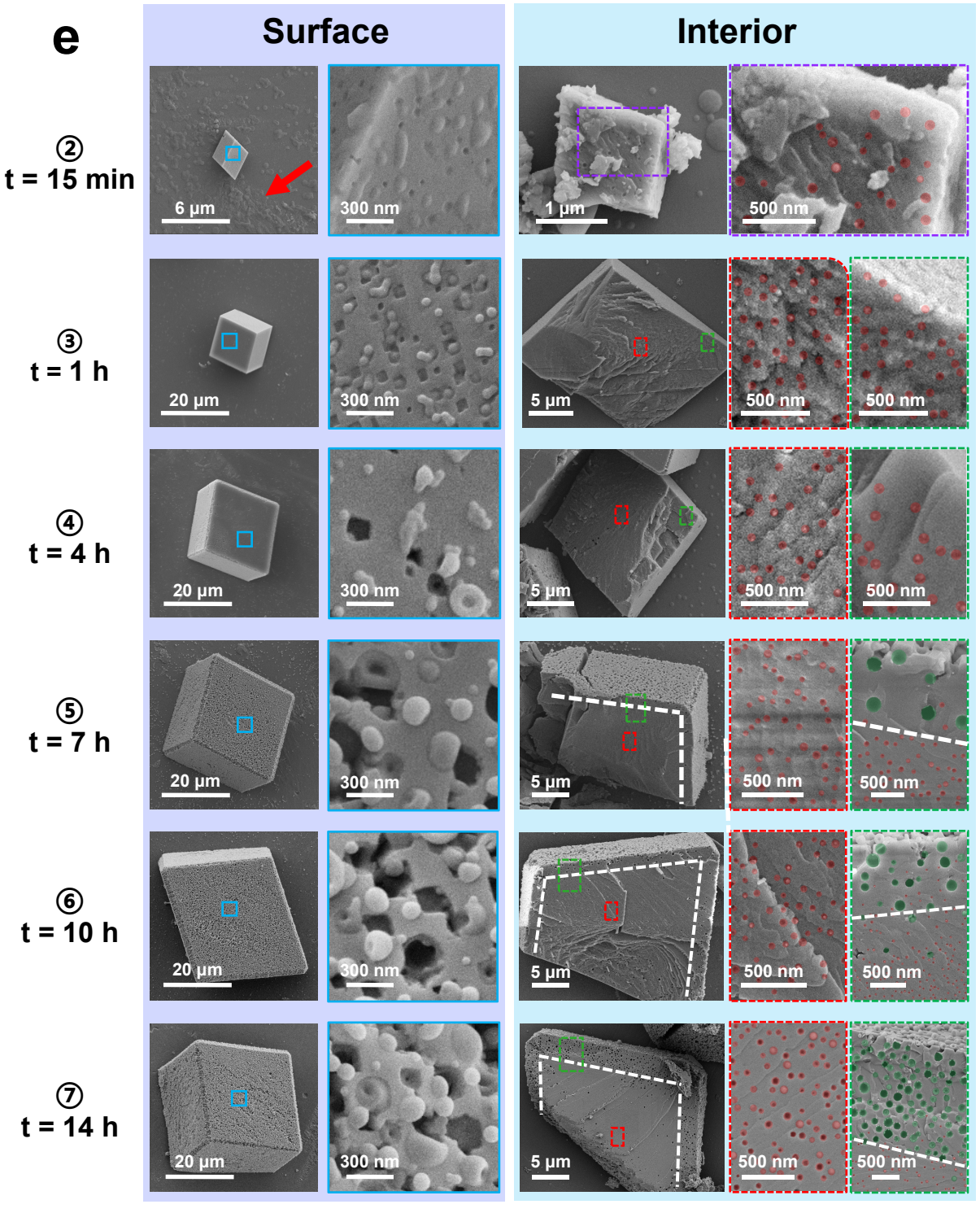
e
Surface
Interior
② t = 15 min
③ t = 1 h
④ t = 4 h
⑤ t = 7 h
⑥ t = 10 h
⑦ t = 14 h
6 μm
300 nm
1 μm
500 nm
20 μm
5 μm

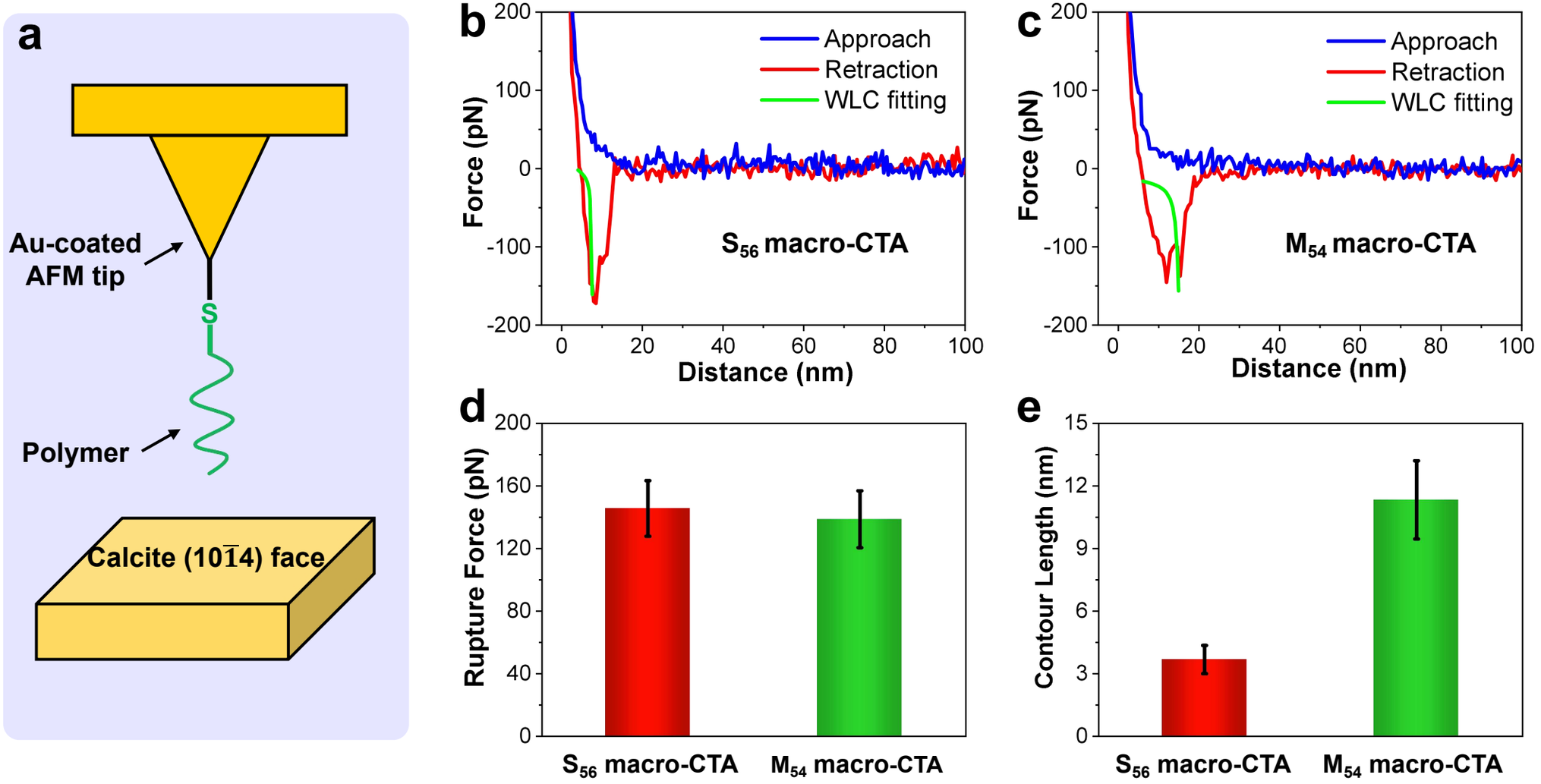
a
Au-coated
AFM tip
S
Polymer
Calcite (10$\bar{1}$4) face
b
Approach
Retraction
WLC fitting
S_{56} macro-CTA
Force (pN)
Distance (nm)
c
Approach
Retraction
WLC fitting
M_{54} macro-CTA
Force (pN)
Distance (nm)
d
Rupture Force (pN)
S_{56} macro-CTA
M_{54} macro-CTA
e
Contour Length (nm)
S_{56} macro-CTA
M_{54} macro-CTA

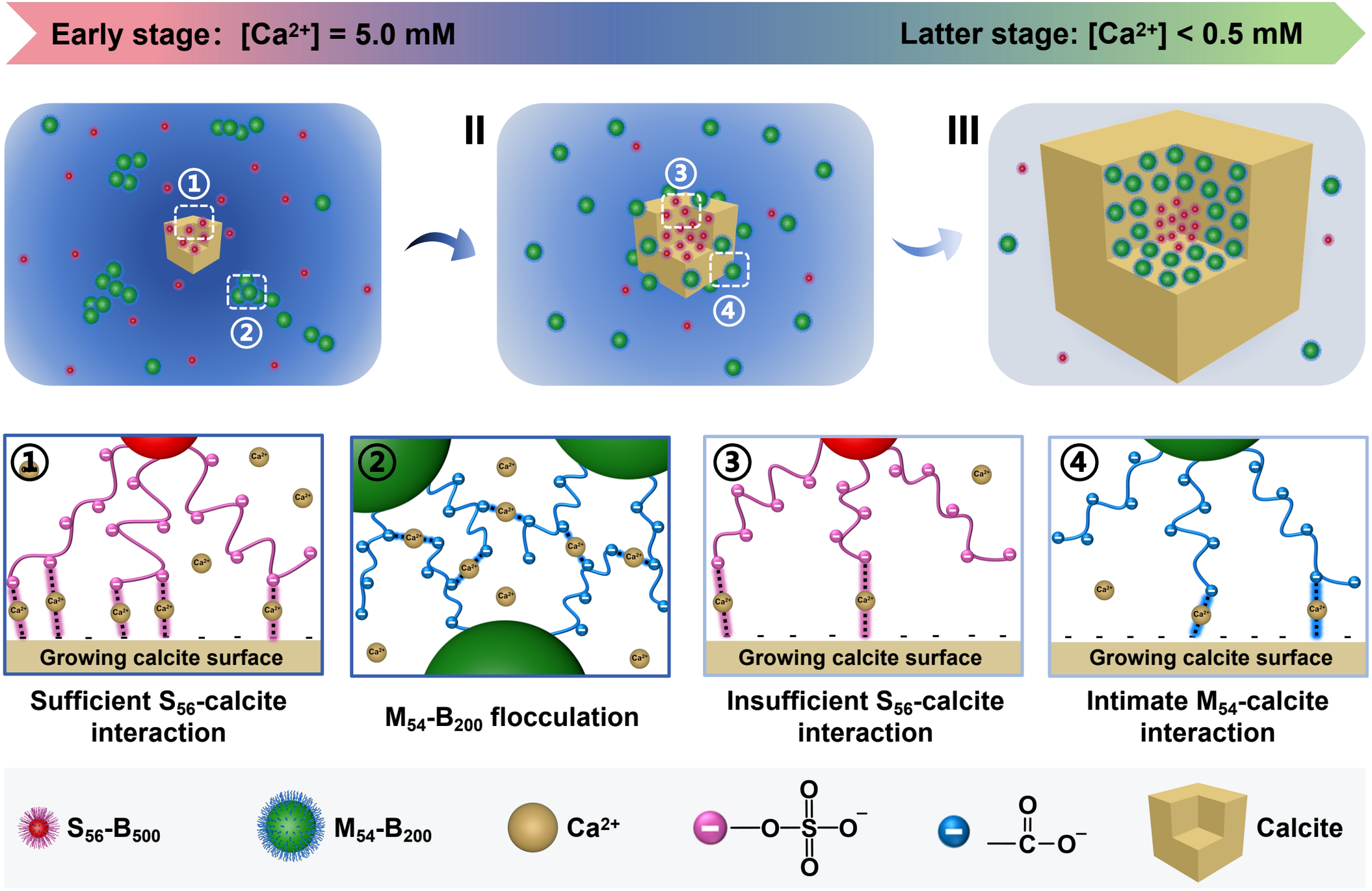
Early stage: [Ca2+] = 5.0 mM
Latter stage: [Ca2+] < 0.5 mM
I
II
III
1
2
3
4
Growing calcite surface
Growing calcite surface
Growing calcite surface
Sufficient S56-calcite interaction
M54-B200 flocculation
Insufficient S56-calcite interaction
Intimate M54-calcite interaction
S56-B500
M54-B200
Ca2+
Calcite

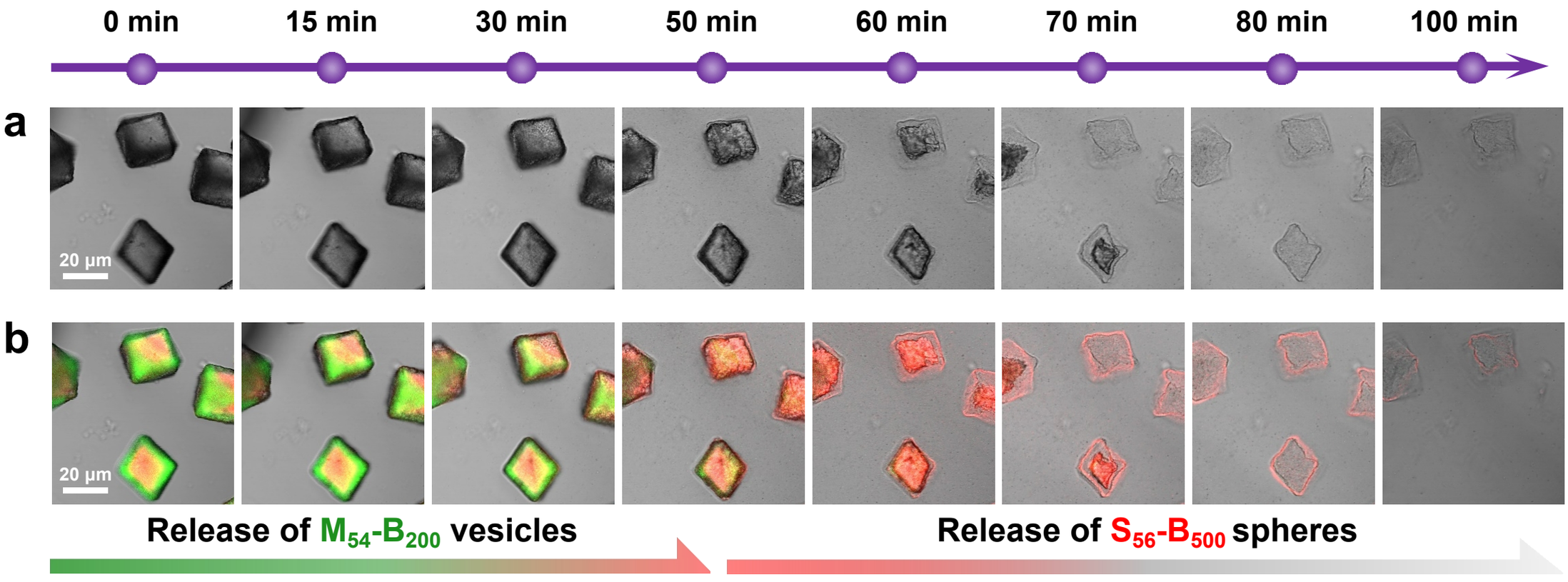
0 min
15 min
30 min
50 min
60 min
70 min
80 min
100 min
a
b
20 μm
20 μm
Release of M54-B200 vesicles
Release of S56-B500 spheres